ORIGINAL PAPER

Second-order wave interaction with a vertical plate

B. Molin · F. Remy · O. Kimmoun

Abstract The second-order interaction of monochromatic water waves with a rigid vertical plate is investigated numerically and experimentally. The plate has a finite width and is projected from one of the side-walls of a wave-tank. This geometry reduces the wave cases to normal incidence but permits a semi-analytical resolution based on eigenfunction expansions. Obtained numerical results are shown to be insensitive to the width of the tank beyond some value, and to converge quickly with the truncation orders of the expansions, in spite of the second-order potential having a logarithmic singularity at the plate edge. Second-order free-surface elevations are compared with values derived from experimental measurements at the BGO-First offshore wave-tank. Good agreement is reported.

Keywords Experimental validation · Potential flow theory · Second-order diffraction · Vertical plate

1 Introduction

For the past twenty or 30 years second-order hydrodynamics has received considerable attention. Numerous contributions have been offered to the resolution of the second-order diffraction problem in regular waves. Semi-analytical solutions have been proposed for particular geometries such as vertical circular cylinders standing on the sea-bottom [1–3] or arrays of vertical cylinders [4]. These are valuable references to be used as benchmarks for numerical models.

It is one purpose of this work to offer another set of reference results, for a different type of body, in the sense that it has a sharp corner (an edge), where the velocity potential is singular. This feature induces numerical difficulties that are absent in the case of circular cylinders. It also creates theoretical problems since, whatever the wave steepness, the right-hand side of the free-surface condition verified by the second-order potential becomes infinite at the plate edge. Physically the flow separates and it is not clear how much and how far local flow separation undermines the potential-flow approach. In this respect comparisons with experimental measurements are valuable.

It is with much pleasure and admiration for his achievements that we dedicate this work to Nick Newman.

B. Molin (✉) · F. Remy · O. Kimmoun
École Généraliste d'Ingénieurs de Marseille, 13 451 Marseille cedex 20, France
e-mail: bernard.molin@egim-mrs.fr

To permit a semi-analytical resolution, we bound the fluid domain by two vertical walls, alike in a wave-tank, with the plate protruding from one of the walls. This geometry limits the applications to normal incidence. When the walls are taken far apart, confinement effects are shown to disappear.

The fluid domain is divided into two sub-domains, up- and down-wave from the plate. In either sub-domain the velocity potentials at first- and second-orders can be expanded over sets of eigenfunctions that satisfy the Laplace equation and the no-flow conditions at the horizontal bottom and at the walls. The problem then reduces to ensuring the no-flow condition at the plate and matching the potentials at the common boundary. Classically, at second-order, the velocity potential is decomposed into a "locked" component, that satisfies the non-homogeneous free-surface condition, and a "free" component that satisfies the homogeneous free-surface condition.

The theoretical developments are described in Sect. 2. Illustrative results are shown in Sect. 3, together with convergence considerations. Comparisons are also shown with experimental results obtained at the offshore tank BGO-First. Good agreement is obtained between measured and calculated second-order free-surface elevations along the plate.

2 Theory

2.1 First-order diffraction problem

Figure 1 illustrates the geometry. Regular incoming waves, of amplitude A_I and frequency ω, propagate from left to right in a channel of width b and waterdepth h. The body consists of a rigid plate of zero thickness, protruding from the wall at the origin of the coordinate system. The plate is standing on the bottom and its width is d.

The diffraction problem is solved in the frequency domain, on the basis that a steady state has been reached. That is, to second-order, the velocity potential is written

$$\Phi(x, y, z, t) = \Re \left\{ \varepsilon \, \varphi^{(1)}(x, y, z) \, \mathrm{e}^{-\mathrm{i}\,\omega t} + \varepsilon^2 \, \varphi^{(2)}(x, y, z) \, \mathrm{e}^{-2\mathrm{i}\,\omega t} \right\} + \varepsilon^2 \, \varphi_0^{(2)}(x, y, z) \tag{1}$$

with $\varepsilon \equiv k \, A_I$ being the wave steepness.

The first-order velocity potential $\varphi^{(1)}$ obeys the Laplace equation in the mean fluid domain $0 \leq y \leq b$; $-h \leq z \leq 0$, the linearized free-surface equation $g \, \partial \varphi^{(1)}/\partial z - \omega^2 \, \varphi^{(1)} = 0$ at $z = 0$, and homogeneous Neumann conditions at the solid boundaries (bottom, walls, plate). On the weather side of the plate it consists in an incoming component, propagating along the channel, and a diffracted component traveling to the left while reflecting on the walls. On the lee side incoming and diffracted components travel to the right.

Fig. 1 Geometry
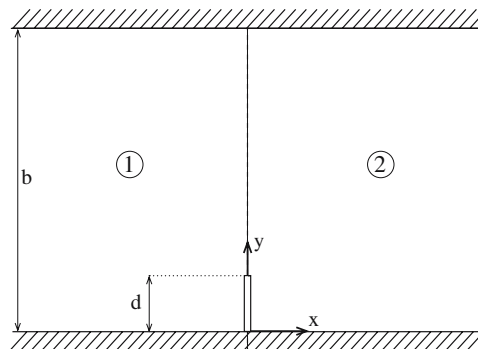
In the left-hand side sub-domain, the first-order velocity potential can be expressed as

$$\varphi_1^{(1)} = A \, \frac{\cosh k \, (z+h)}{\cosh kh} \, \left\{ e^{ikx} + \sum_{n=0}^{\infty} B_n \, e^{-i\alpha_n x} \, \cos \lambda_n y \right\} \tag{2}$$

and in the right-hand side sub-domain

$$\varphi_2^{(1)} = A \, \frac{\cosh k \, (z+h)}{\cosh kh} \, \left\{ e^{ikx} + \sum_{n=0}^{\infty} C_n \, e^{i\alpha_n x} \, \cos \lambda_n y \right\} \tag{3}$$

with $A = -i \, A_I g / \omega$, k the wave number linked to the frequency ω by the dispersion equation $\omega^2 = g \, k \, \tanh kh$, and

$$\alpha_n = \sqrt{k^2 - \lambda_n^2} \quad n = 0, N, \tag{4}$$

$$\alpha_n = i \, \sqrt{\lambda_n^2 - k^2} \quad n = N+1, \infty. \tag{5}$$

Here $\lambda_n = n \, \pi / b$ and N is the largest integer n such that k is larger than λ_n. For $n \leq N$ the modes are progressive; for $n > N$, they are evanescent.

Expressions (2) and (3) ensure that the Laplace equation and the no-flow conditions at the bottom and at the walls are fulfilled. The diffracted waves are outgoing from the common boundary $x = 0$ with reflections on the side-walls.

The remaining conditions to be fulfilled, in $x = 0$, are the no-flow condition on the plate ($0 \leq y \leq d$) and matching conditions from the plate edge to the exterior wall ($d \leq y \leq b$):

$$\frac{\partial \varphi_1^{(1)}}{\partial x} = \frac{\partial \varphi_2^{(1)}}{\partial x} = 0 \quad \text{for } 0 \leq y \leq d, \tag{6}$$

$$\varphi_1 = \varphi_2 \quad \text{for } d \leq y \leq b, \tag{7}$$

$$\frac{\partial \varphi_1^{(1)}}{\partial x} = \frac{\partial \varphi_2^{(1)}}{\partial x} \quad \text{for } d \leq y \leq b. \tag{8}$$

Since $\partial \varphi_1^{(1)} / \partial x = \partial \varphi_2^{(1)} / \partial x$ all over the width of the tank and the $\cos \lambda_n y$ functions form an orthogonal set over $[0 \ b]$, it results that $C_n \equiv -B_n$. The remaining conditions reduce to

$$\sum_{n=0}^{\infty} \alpha_n \, B_n \, \cos \lambda_n y = k \quad 0 \leq y \leq d, \tag{9}$$

$$\sum_{n=0}^{\infty} B_n \, \cos \lambda_n y = 0 \quad d \leq y \leq b. \tag{10}$$

These equations are written under the form

$$B_m \, \cos \lambda_m y + \sum_{n \neq m} \frac{\alpha_n}{\alpha_m} \, B_n \, \cos \lambda_n y = \frac{k}{\alpha_m} \quad 0 \leq y \leq d, \tag{11}$$

$$B_m \, \cos \lambda_m y + \sum_{n \neq m} B_n \, \cos \lambda_n y = 0 \quad d \leq y \leq b. \tag{12}$$

Both sides of both equations are multiplied by $\cos \lambda_m y$, integrated in y over their domains of validity, and added up, resulting into the linear system:

$$B_m \, \frac{(1 + \delta_{0m}) \, b}{2} + \sum_{n \neq m} \left(\frac{\alpha_n}{\alpha_m} - 1 \right) \, B_n \int_0^d \cos \lambda_m y \, \cos \lambda_n y \, \mathrm{d}y = \frac{k}{\alpha_m \, \lambda_m} \, \sin \lambda_m d \tag{13}$$

with δ_{ij} the Kronecker symbol.

This system is solved by a standard Gauss routine.

2.2 Second-order diffraction problem

The second-order potential $\varphi^{(2)}$ at the double frequency $2\,\omega$ obeys the free-surface condition in $z = 0$:

$$g\,\varphi_z^{(2)} - 4\,\omega^2\,\varphi^{(2)} = \mathrm{i}\,\omega \left[\varphi_x^{(1)2} + \varphi_y^{(1)2} + \varphi_z^{(1)2} - \frac{1}{2g}\,\varphi^{(1)}\left(g\,\varphi_{zz}^{(1)} - \omega^2\,\varphi_z^{(1)}\right)\right] \tag{14}$$

or

$$g\,\varphi_z^{(2)} - 4\,\omega^2\,\varphi^{(2)} = \mathrm{i}\,\omega \left[\varphi_x^{(1)2} + \varphi_y^{(1)2} + \frac{1}{2}\,k^2\,T\,\varphi^{(1)2}\right] \tag{15}$$

with $T = 3\tanh^2 kh - 1$.

   We follow the usual technique of decomposing the second-order potential into a particular component that satisfies the non-homogeneous free surface condition and a "free" component that verifies the no-flow condition on the plate and takes care of the matching conditions at the common boundary.

2.2.1 Locked potential in sub-domain 1

After calculations the right-hand side of Eq. 15 is obtained as

$$\frac{g\,\varphi_z^{(2)} - 4\,\omega^2\,\varphi^{(2)}}{\mathrm{i}\,\omega\,A^2} = -\frac{3\,k^2}{2\cosh^2 kh}\,\mathrm{e}^{2\mathrm{i}\,k x} + \sum_{n=0}^{\infty}[k^2\,T + 2\,k\alpha_n]\,B_n\,\mathrm{e}^{\mathrm{i}\,(k-\alpha_n)x}\,\cos\lambda_n y$$

$$+\frac{1}{4}\sum_{m=0}^{\infty}\sum_{n=0}^{\infty}\left\{\left[k^2\,T - 2\alpha_m\alpha_n - 2\lambda_m\lambda_n\right]\cos(\lambda_m + \lambda_n)y + \left[k^2\,T - 2\alpha_m\alpha_n + 2\lambda_m\lambda_n\right]\right.$$

$$\left. \times\cos(\lambda_m - \lambda_n)y\right\}B_m\,B_n\,\mathrm{e}^{-\mathrm{i}\,(\alpha_m+\alpha_n)x} \tag{16}$$

   A particular solution $\varphi_{L1}^{(2)}$ can be looked for as the sum of three terms:

$$\varphi_{L1}^{(2)} = \varphi_I^{(2)} + \varphi_{L12}^{(2)} + \varphi_{L13}^{(2)}. \tag{17}$$

with $\varphi_I^{(2)}$ the second-order incident potential, given by

$$\varphi_I^{(2)} = -\frac{3\,\mathrm{i}}{8}\,\frac{A_I^2\,\omega}{\sinh^4 kh}\,\cosh 2k\,(z+h)\,\mathrm{e}^{2\mathrm{i}\,k x} \tag{18}$$

and

$$\varphi_{L12}^{(2)} = \sum_{n=0}^{\infty}\beta_n\,\mathrm{e}^{\mathrm{i}\,(k-\alpha_n)x}\,\cos\lambda_n y\,\frac{\cosh\nu_n(z+h)}{\cosh\nu_n h} \tag{19}$$

with

$$\nu_n^2 = 2\,k^2 - 2\,k\,\alpha_n, \tag{20}$$

$$\beta_n = \frac{\mathrm{i}\,\omega\,k\,A^2\,[k\,T + 2\,\alpha_n]\,B_n}{g\,\nu_n\,\tanh\nu_n h - 4\,\omega^2} \tag{21}$$

and

$$\varphi_{L13}^{(2)} = \sum_{m=0}^{\infty}\sum_{n=0}^{\infty}\gamma_{mn1}\,\mathrm{e}^{-\mathrm{i}\,(\alpha_m+\alpha_n)x}\,\cos(\lambda_m + \lambda_n)y\,\frac{\cosh\mu_{mn1}(z+h)}{\cosh\mu_{mn1}h}$$

$$+\sum_{m=0}^{\infty}\sum_{n=0}^{\infty}\gamma_{mn2}\,\mathrm{e}^{-\mathrm{i}\,(\alpha_m+\alpha_n)x}\,\cos(\lambda_m - \lambda_n)y\,\frac{\cosh\mu_{mn2}(z+h)}{\cosh\mu_{mn2}h}, \tag{22}$$

where

$$\mu_{mn1}^2 = (\alpha_m + \alpha_n)^2 + (\lambda_m + \lambda_n)^2, \tag{23}$$

$$\mu_{mn2}^2 = (\alpha_m + \alpha_n)^2 + (\lambda_m - \lambda_n)^2, \tag{24}$$

$$\gamma_{mn1} = \frac{\mathrm{i}\,\omega\,A^2\,[k^2\,T - 2\lambda_m\lambda_n - 2\alpha_m\alpha_n]\,B_m\,B_n}{4\,(g\,\mu_{mn1}\,\tanh\mu_{mn1}h - 4\,\omega^2)}, \tag{25}$$

$$\gamma_{mn2} = \frac{\mathrm{i}\,\omega\,A^2\,[k^2\,T + 2\lambda_m\lambda_n - 2\alpha_m\alpha_n]\,B_m\,B_n}{4\,(g\,\mu_{mn2}\,\tanh\mu_{mn2}h - 4\,\omega^2)}. \tag{26}$$

It can be noted that the wave numbers ν_n and μ_{mn2} are complex, while μ_{mn1} is real.

2.2.2 Locked potential in sub-domain 2

Similarly a particular solution is obtained as

$$\varphi_{L2}^{(2)} = \varphi_I^{(2)} + \varphi_{L22}^{(2)} + \varphi_{L23}^{(2)} \tag{27}$$

with

$$\varphi_{L22}^{(2)} = \sum_{n=0}^{\infty} \widetilde{\beta}_n\,\mathrm{e}^{\mathrm{i}\,(k-\alpha_n)\,x}\,\cos\lambda_n y\,\frac{\cosh\widetilde{\nu}_n(z+h)}{\cosh\widetilde{\nu}_n h}, \tag{28}$$

$$\widetilde{\nu}_n^2 = (k+\alpha_n)^2 + \lambda_n^2, \tag{29}$$

$$\widetilde{\beta}_n = \frac{\mathrm{i}\,\omega\,k\,A^2\,[2\,\alpha_n - k\,T]\,B_n}{g\,\widetilde{\nu}_n\,\tanh\widetilde{\nu}_n h - 4\,\omega^2} \tag{30}$$

and

$$\varphi_{L23}^{(2)} = \sum_{m=0}^{\infty}\sum_{n=0}^{\infty}\gamma_{mn1}\,\mathrm{e}^{\mathrm{i}\,(\alpha_m+\alpha_n)x}\,\cos(\lambda_m+\lambda_n)y\,\frac{\cosh\mu_{mn1}(z+h)}{\cosh\mu_{mn1}h}$$

$$+ \sum_{m=0}^{\infty}\sum_{n=0}^{\infty}\gamma_{mn2}\,\mathrm{e}^{\mathrm{i}\,(\alpha_m+\alpha_n)x}\,\cos(\lambda_m-\lambda_n)y\,\frac{\cosh\mu_{mn2}(z+h)}{\cosh\mu_{mn2}h}. \tag{31}$$

2.2.3 Free wave components

In either sub-domain we must add up free waves in order to fulfill the boundary and matching conditions in $x=0$.

In the left-hand side sub-domain the free wave potential is expressed as

$$\varphi_{F1}^{(2)} = \sum_{m=0}^{\infty}\cos\lambda_m y\,\left[D_{m0}\,\mathrm{e}^{-\mathrm{i}\,r_{m0}\,x}\,\frac{\cosh k_{20}(z+h)}{\cosh k_{20}h} + \sum_{n=1}^{\infty}D_{mn}\,\mathrm{e}^{r_{mn}x}\,\cos k_{2n}(z+h)\right], \tag{32}$$

where

$$4\,\omega^2 = g\,k_{20}\,\tanh k_{20}h = -g\,k_{2n}\,\tan k_{2n}h \tag{33}$$

and

$$r_{m0}^2 = k_{20}^2 - \lambda_m^2 \quad r_{mn} = \sqrt{k_{2n}^2 + \lambda_m^2}. \tag{34}$$

In the right-hand side sub-domain the free wave potential is expressed as

$$\varphi_{F2}^{(2)} = \sum_{m=0}^{\infty}\cos\lambda_m y\,\left[E_{m0}\,\mathrm{e}^{\mathrm{i}\,r_{m0}\,x}\,\frac{\cosh k_{20}(z+h)}{\cosh k_{20}h} + \sum_{n=1}^{\infty}E_{mn}\,\mathrm{e}^{-r_{mn}x}\,\cos k_{2n}(z+h)\right]. \tag{35}$$

2.3 Matching

To satisfy the no-flow condition on the plate and matching conditions in $x = 0$, we take advantage that the $\cosh k_{20}(z + h)/\cosh k_{20}h$, $\cos k_{2n}(z + h)$ functions provide an orthogonal set in z over $[-h \quad 0]$. We project the locked components over this basis. This yields independent two-dimensional problems (in (x, y)), similar to the first-order problem.

3 Results

3.1 Convergence study

We take a geometry inspired from the square cylinder studied in [5]. We replace the square cylinder by a plate of equal width. We refer to the case $kh = 3$ in [5]. So we take a plate width d of 1 m, a waterdepth h of 1 m and a wavelength of 2.0944 m.

First we investigate the effects of series truncation and tank width on the first-order elevation along the plate, on its weather side. Figure 2 shows the obtained RAOs for a channel width of 10 m and truncation orders of 100, 200 and 400, and for a channel width of 15 m and a truncation order of 200. The plots are extended to twice the width of the plate to check that the RAOs are equal to one when $y \geq d$. It can be observed that the curves are hardly distinguishable when the truncation order is larger than 200.

We now consider the second-order potential along the same strip ($x = 0^{-}$; $0 \leq y \leq 2$). We take the tank width equal to 10 m, truncation order $N = NY$ in y equal to 200 and we vary the truncation order in z of the second-order free waves from 25 up to 100. The same truncation order NY in y is taken for the first-order and second-order potentials. The second-order potential is made non-dimensional in the same fashion as in [5], that is in the form $2\omega |\varphi^{(2)}(0^{-}, y, 0)| (2d)/(gA^2)$. Results are shown in Fig. 3 where it can be observed that 50 and 100 provide quasi-identical curves.

In Fig. 4 we keep the truncation order NZ equal to 50 and we vary NY from 100 to 400. It can be observed that $NY = 200$ and $NY = 400$ provide quasi-identical results, except by the plate edge where the second-order potential is singular: as the truncation order is increased, the singularity starts appearing as a sharp peak. It is shown in the Appendix that the singularity is logarithmic. Fortunately it is quite localized and the $NY = 200$ and $NY = 400$ curves coalesce together at short distance from the plate edge.

In Figs. 5–8 we show bird's eye views of the (normalized) second-order potential in the vicinity of the plate. First the imaginary parts of the locked (Fig. 5) and free components (Fig. 6), then their sum (Fig. 7). Figure 8 shows the real part of the second-order potential, with a change in sign, to make apparent the peak at the plate edge, due to the logarithmic singularity. The truncation orders NY and NZ have been

Fig. 2 First-order free-surface elevation. $kh = 3$; $k \times (2d) = 6$. Sensitivity to truncation order and tank width
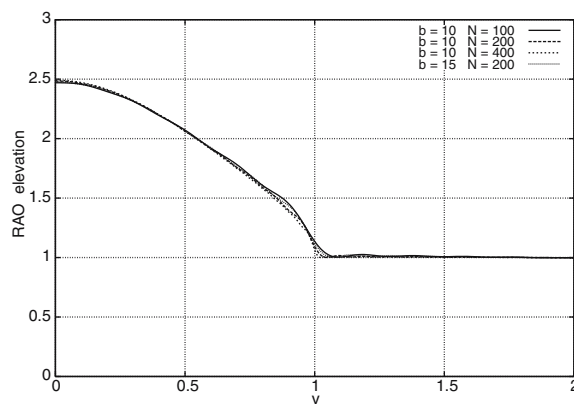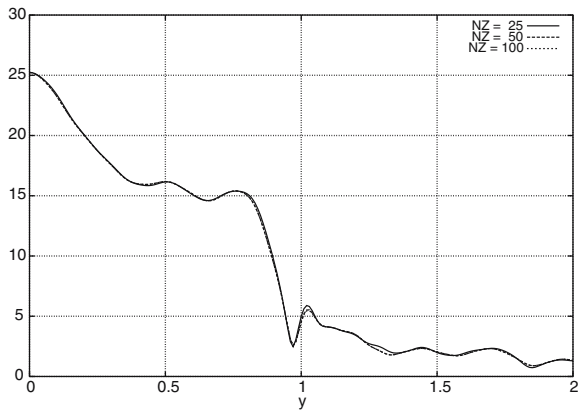
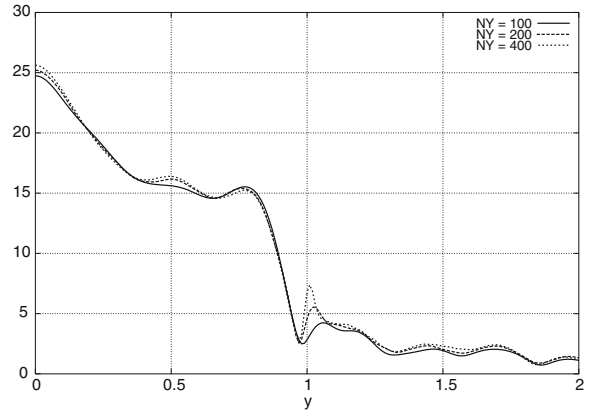**Fig. 3** Second-order potential. $kh = 3$; $k \times (2d) = 6$. Basin width: 10 m. $NY = 200$

Fig. 4 Second-order potential. $kh = 3$; $k \times (2d) = 6$. Basin width: 10 m. $NZ = 50$
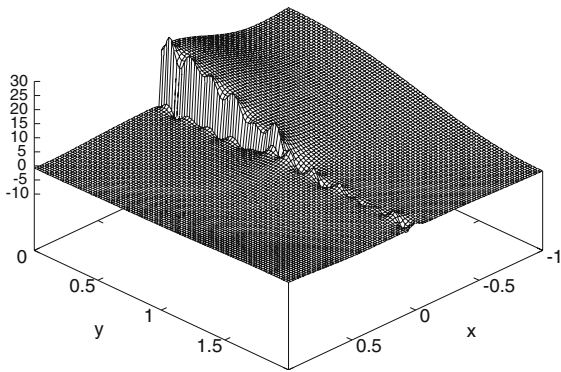

Fig. 5 Three-dimensional view of the second-order potential at the free surface. Locked component. Imaginary part. Basin width: 10 m. $NZ = 50$; $NY = 200$
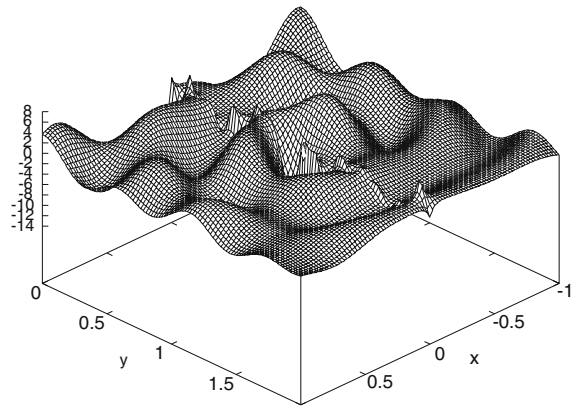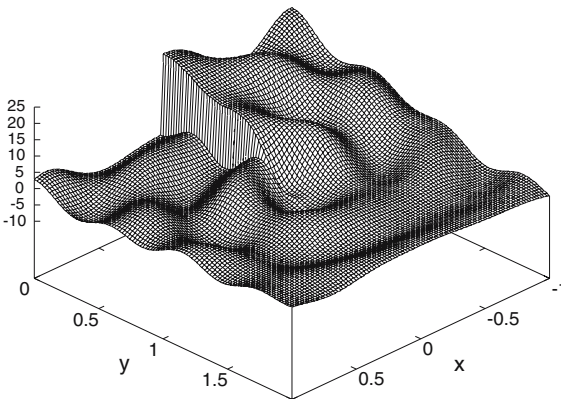
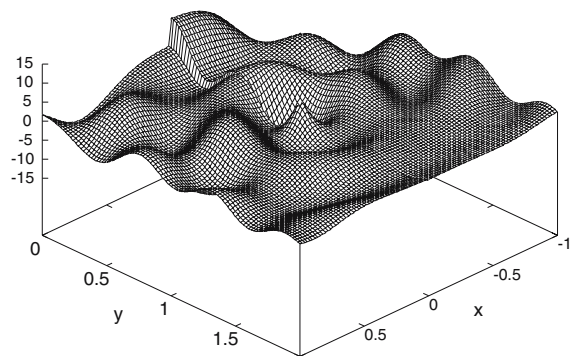**Fig. 6** Three-dimensional view of the second-order potential at the free surface. Free component. Imaginary part. Basin width: 10 m. $NZ = 50$; $NY = 200$

Fig. 7 Three-dimensional view of the second-order potential at the free surface. Locked plus free components. Imaginary part. Basin width: 10 m. $NZ = 50$; $NY = 200$

Fig. 8 Three-dimensional view of the second-order potential at the free surface. Locked + free components. Real part (changed in sign). Basin width: 10 m. $NZ = 50$; $NY = 200$
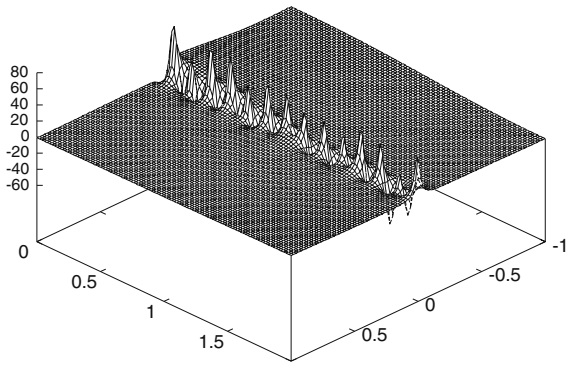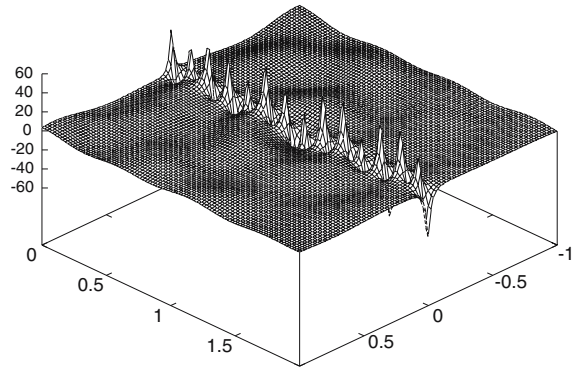
Fig. 9 Three-dimensional view of the second-order potential at the free surface. Locked component. Imaginary part. Basin width: 12.5 m. $NZ = 50$; $NY = 250$

Fig. 10 Three-dimensional view of the second-order potential at the free surface. Free component. Imaginary part. Basin width: 12.5 m. $NZ = 50$; $NY = 250$
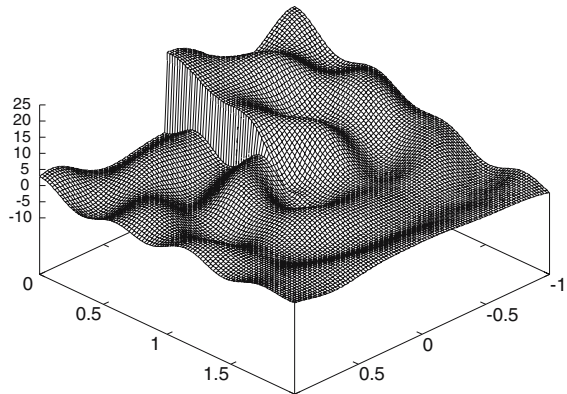

Fig. 11 Three-dimensional view of the second-order potential at the free surface. Locked + free components. Imaginary part. Basin width: 12.5 m. $NZ = 50$; $NY = 250$
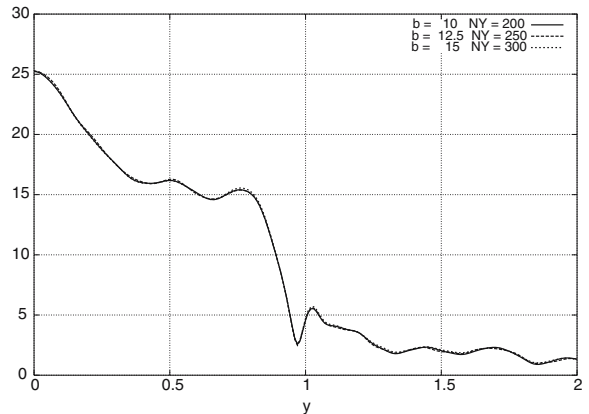

Fig. 12 Second-order potential in $x = 0^-$ for different tank widths. $kh = 3$; $k \times (2d) = 6$

taken equal to 200 and 50, respectively. It can be checked visually, in Figs. 7 and 8, that the matching at $x = 0$; $y > d$ is excellent.

Finally Figs. 9–11 show similar views as Figs. 5–7, for a basin width of 12.5 m. The truncation order NY has been increased from 200 to 250 to keep the same spatial resolution. It must be pointed out here that 10 and 12.5 m are the specified values. They are slightly modified in the code so that they be an integer +0.5 times the half wavelength of the second-order free waves, to avoid resonant transverse modes. So 10 m is changed into 10.0793, and 12.5 m is changed into 12.4355 m. Even though the first-order elevations along the matching strip ($x = 0$; $y > d$) differ by less than 0.2%, the high-frequency contents of the locked and free components are quite different. This may be related to the fact that the wave numbers of the participating modes are different. In particular, the number of progressive modes is 9 at the 10 m tank width and 11 at the 12.5 m one. It must also be borne in mind that the decomposition into locked and free components is not unique. When the locked and free components are added up, the same patterns as in the 10 m width case are obtained, as confirmed by Fig. 12, where we also show the curve obtained for a width of 15 m (15.0535 m) and $NY = 300$.
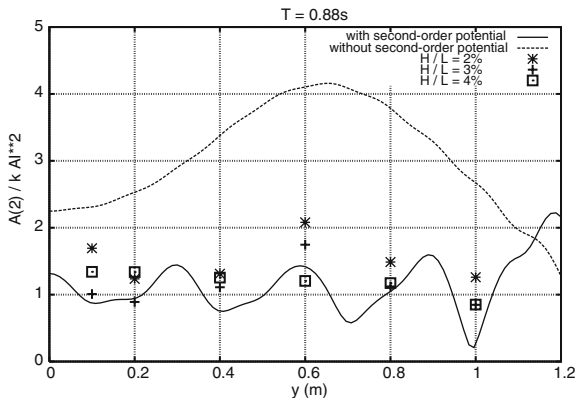
Fig. 13 Second-order elevation along the plate. Comparison between numerical and experimental values. Wave period: 0.88 s
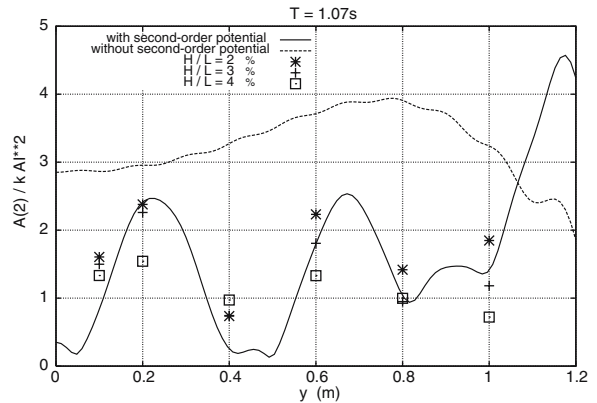

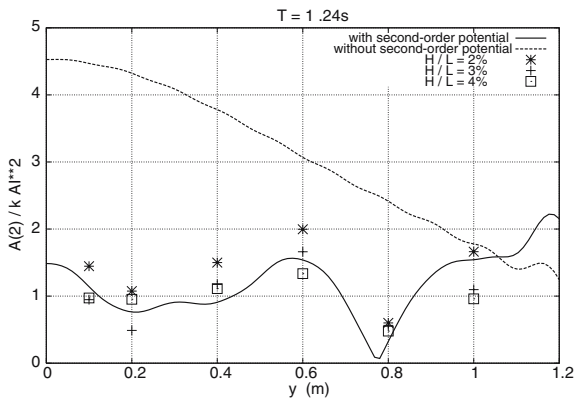**Fig. 14** Same as Fig. 13. Wave period: 1.07 s

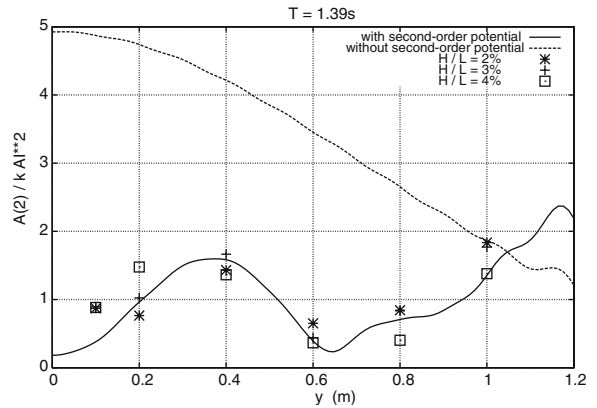**Fig. 15** Same as Fig. 13. Wave period: 1.24 s

Fig. 16 Same as Fig. 13. Wave period: 1.39 s

3.2 Comparisons with experimental measurements

We now present some comparisons with second-order elevations derived from tests at BGO-First in la Seyne-sur-mer. The plate, attached to one of the side-walls, has a width d of 1.2 m, a thickness of 5 cm and a draft of 1.5 m, in a waterdepth of 3 m. The instrumentation consists in capacitive wave gauges along the weather side of the plate, at 10, 20, 40, 60, 80 and 100 cm from the wall.

The plate is submitted to regular waves of periods 0.88, 0.98, 1.07, 1.16, 1.24, 1.32 and 1.39 s, meaning wavelengths (for small amplitude waves) of 1.2, 1.5, 1.8, 2.1, 2.4, 2.7 and 3 m. Wave steepnesses H/L (wave-height over wavelength ratio) from 2 up to 6% are achieved. Further details on the tests can be found in [6].

The double-frequency component was extracted from the time series via Fourier analysis over a time window chosen a short time after arrival of the wave front (to minimize the third-order run-up effect).

As for the calculations, the theoretical second-order elevation is given by

$$\eta^{(2)} = -\frac{1}{g}\,\eta^{(1)}\,\Phi_{zt}^{(1)} - \frac{1}{2g}\,\nabla\Phi^{(1)}\cdot\nabla\Phi^{(1)} - \frac{1}{g}\,\Phi_t^{(2)}\bigg|_{z=0}. \tag{36}$$
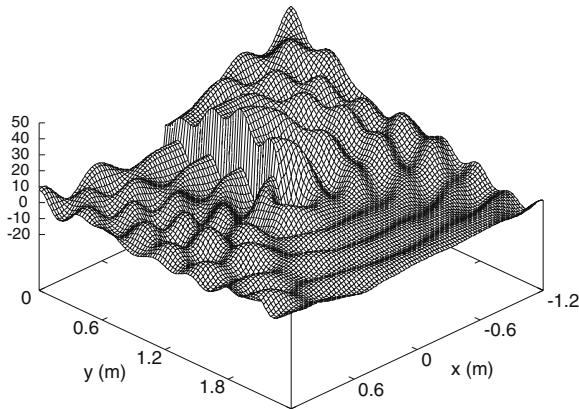
Fig. 17 Three-dimensional view of the second-order potential at the free surface. Imaginary part. Wave period: 0.88 s
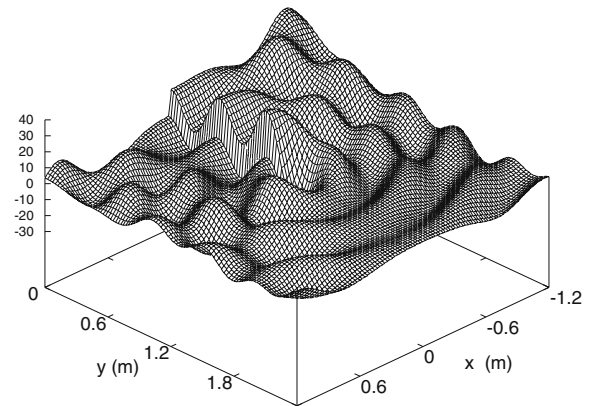
Fig. 18 Same as Fig. 17. Wave period: 1.07 s

The double-frequency component can be expressed as

$$\eta_2^{(2)} = \Re\mathfrak{e}\left\{\left[\frac{2\,\mathrm{i}\,\omega}{g}\,\varphi^{(2)} - \frac{3\,\omega^4}{4\,g^3}\,\varphi^{(1)2} - \frac{1}{4\,g}\,\left(\varphi_x^{(1)2} + \varphi_y^{(1)2}\right)\right]\,\mathrm{e}^{-2\,\mathrm{i}\,\omega\,t}\right\}\bigg|_{z=0}. \tag{37}$$

Figures 13–16 present comparisons between the numerical and experimental values at wavelengths of 1.2, 1.8, 2.4 and 3 m. The double-frequency elevations are normalized by $k\,A_I^2$, where k is the wave number and A_I the fundamental component of the amplitude of the incoming waves. Experimental values are derived from the measurements at the smaller wave steepnesses H/L of 2, 3 and 4%. At higher steepnesses the run-up effect quickly appears, rendering the analysis impossible. In the numerical computations the basin width was taken equal to 12 m (10 times the plate width), the waterdepth equal to half a wavelength, and the truncation orders NY and NZ equal to 200 and 50, for all wave periods. In the figures calculated results are shown with and without the second-order potential included, to stress out its significance.

It can be seen that the agreement between numerical predictions and measurements is rather good. This is true even at the wave gauge closest to the plate edge, showing that flow separation has limited effects on the neighboring free surface.

Finally Figs. 17 and 18 show three-dimensional views of the imaginary parts of the second-order potential, around the plate, at the wave periods of 0.88 and 1.07 s. They are normalized in the same fashion as in the previous section. Quite complicated patterns are obtained as such low wavelengths.

4 Concluding remarks

It is noteworthy that, in spite of the sharp edge that induces flow separation in the physical tank and a strong singularity in the potential idealization, good agreement has been finally reported between measured and calculated values of the free-surface elevations, to second-order, even at rather short distances from the plate edge. This proves that non-potential flow effects are confined to a rather small neighborhood of the edge.

Problems of numerical convergence, with respect to the truncation orders of the series, were expected at the initiation of this study. They turned out to be less pronounced than feared, when one considers, not the locked or free wave potentials separately, but their sum.

Appendix. Singularity at the plate edge

In this appendix we determine the singularity of the second-order potential at the plate edge.

The singularity at first-order is well known: the potential $\varphi^{(1)}$ behaves locally as $\sqrt{R}$ with $R = \sqrt{x^2 + (y-d)^2}$ the horizontal distance from the plate edge. So the horizontal velocity squared behaves as $1/R$, while the vertical velocity remains finite. Hence, to the leading order, the free-surface equation satisfied by $\varphi^{(2)}$ in the vicinity of the plate edge can be written

$$g\,\varphi_z^{(2)} - 4\,\omega^2\,\varphi^{(2)} = \mathrm{i}\,\omega A^2\,\frac{\alpha(\omega)}{R} = \mathrm{i}\,\omega A^2\,\alpha\,\int_0^\infty J_0(\nu R)\,\mathrm{d}\nu \tag{38}$$

with α a complex constant and J_0 the Bessel function of the first kind and order zero.

A solution for $\varphi^{(2)}$ (assuming infinite waterdepth for the sake of simplicity), is

$$\varphi^{(2)}(R,z) = \frac{\mathrm{i}\,\omega A^2\,\alpha}{g}\,\int_0^\infty \frac{J_0(\nu R)}{\nu - k_{20}}\,\mathrm{e}^{\nu z}\,\mathrm{d}\nu, \tag{39}$$

where the integration contour at the pole k_{20} must ensure that the radiation condition is satisfied. We get

$$\varphi^{(2)}(R,z) = \frac{\mathrm{i}\,\omega A^2\,\alpha}{g}\,\left[\mathrm{P.V.}\int_0^\infty \frac{J_0(\nu R)}{\nu - k_{20}}\,\mathrm{e}^{\nu z}\,\mathrm{d}\nu + \mathrm{i}\,\pi\,J_0(k_{20}R)\,\mathrm{e}^{k_{20}\,z}\right] \tag{40}$$

in agreement with [7, Eq. 21.6] (with a correction in sign). This represents a flow which is radial from the plate edge. Hence the plate is transparent to this flow.

At the free surface ($z = 0$), the principal valued integral can be transformed into

$$\mathrm{P.V.}\int_0^\infty \frac{J_0(u)}{u - k_{20}\,R}\,\mathrm{d}u, \tag{41}$$

which is easily shown to behave as $-\log(k_{20}R)$ for $k_{20}R \to 0$.

Hence $\varphi^{(2)}$ has a logarithmic singularity at the plate edge.

References

1. Chau FP, Eatock Taylor R (1992) Second order wave diffraction by a vertical cylinder. J Fluid Mech 240:571–599
2. Malenica Š, Molin B (1995) Third harmonic wave diffraction by a vertical cylinder. J Fluid Mech 302:203–229
3. Newman JN (1996) The second-order wave force on a vertical cylinder. J Fluid Mech 320:417–443
4. Malenica Š, Eatock Taylor R, Huang JB (1999) Second-order wave diffraction by an array of vertical cylinders. J Fluid Mech 390:349–373
5. Molin B, Jamois E, Lee CH, Newman JN (2005) Non-linear wave interaction with a square cylinder. In: Grue J (ed) Proc. 20th int. workshop water waves & floating bodies. Longyearbyen
6. Molin B, Remy F, Kimmoun O, Jamois E (2005) The role of tertiary wave interactions in wave-body problems. J Fluid Mech 528:323–354
7. Wehausen JV, Laitone EV (1960) Surface waves. Handbuch der Phys 9:446–777